properties of metal ion centers in proteins and enzymes cannot be adequately described on the basis of idealized model systems.

The optical spectra of coordination compounds may be classified in general into ligand field bands and charge-transfer bands. The visible absorption spectra of high-spin Co^{2+} complexes in low-symmetry sites have been interpreted only in terms of intense ligand field transitions.[4-11] This tradition has been continued in textbooks of the spectroscopy of inorganic coordination complexes in which the intensity in the visible region of spectra of high-spin tetrahedral Co^{2+} complexes is ascribed to ligand field transitions with 3d-4p mixing.[45,46] The classical study of Ballhausen and Liehr[12] demonstrated that d-p mixing due to the tetrahedral crystal field is insufficient as a mechanism of intensity to account for the visible absorption spectra of tetrahedral complexes of high-spin Co^{2+}. Similarly, on the basis of the EH molecular orbital model, metal p orbitals are not involved in optical transitions. As shown in Table III, there are small contributions of metal p functions in the highest singly occupied orbitals 19, 20, and 21. However, the lower energy, doubly occupied orbital 26, from which transitions best account for the intensity in the visible region, has no metal p orbital contribution. Of the three possible quartet-allowed electron promotions from orbital 24 with a small fraction of metal p function, the transition 24 → 20 is symmetry forbidden; the value of Q is zero for 24 → 19; and the one-electron promotion 24 → 21 yields an estimated oscillator strength of 7.5×10^{-4}, insignificant in comparison to those from orbital 26 with mixing of only ligand and metal d wave functions. Moreover, the orbitals 28, 30, and 31, which account best for the more intense, near-ultraviolet bands, have no metal p contributions. The results of our EH calculations show that the most intense optical bands in the visible and near-ultraviolet regions can be accounted for best from the mixing of either sulfur or nitrogen orbitals into the lower and upper molecular orbitals associated with optical transitions and that not only the bands in the near-ultraviolet but also the bands in the visible region are predominantly of charge-transfer character. On the other hand, the weak bands in the near-infrared region are clearly consistent according to both energy and intensity with assignment to transitions involving primarily the metal d orbitals.

It is, moreover, of interest to note that the choice of parameters for our EH calculations to predict energies and relative intensities of ligand → metal charge-transfer transitions was restricted to the set generally employed by others[32,33] without further adjustment to obtain agreement between theory and experiment. Also, coefficients for the double-ζ expansion of the Slater exponents for 3d functions[33] were not employed. The EH results yielded in each case remarkably good agreement with observed spectra, consistent with our previous experience in the assignment of heme optical spectra on the basis of polarized single crystal spectra and EH molecular orbital models.[25-29] This approach of assigning the orbital origins of the spectrum on the combined basis of polarized single crystal spectroscopic data and molecular orbital models, therefore, should be suitable to investigate further the influence of changes in metal coordination environment, particularly with respect to donor ligand atoms and coordination number as may occur in the enzyme-catalyzed reaction.[17,47]

Registry No. $Co(SCH_3)_2(NH_3)_2$, 108122-73-2; $Co(SCH_3)_2(NH_3)(H_2O)$, 108122-74-3; $Co(SCH_3)_2(imidazole)_2$, 108122-75-4; $Co(SCH_3)_2(imidazole)(H_2O)$, 108122-76-5.

(44) (a) Vallee, B. L.; Williams, R. J. P. *Proc. Natl. Acad. Sci. U.S.A.* **1968**, *59*, 498-502. (b) Williams, R. J. P. *Cold Spring Harbor Symp. Quant. Biol.* **1972**, *36*, 53-62. (c) Vallee, B. L.; Galdes, A. In *Advances in Enzymology and Related Areas of Molecular Biology*; Meister, A., Ed.; Wiley: New York, 1984; pp 283-430.

(45) Lever, A. B. P. *Inorganic Electronic Spectroscopy*; Elsevier: New York, 1984; pp 480-505.

(46) Williams, A. F. *A Theoretical Approach to Inorganic Chemistry*; Springer Verlag: Berlin, 1979; Chapter 4, pp 132-158.

(47) Yim, M. B.; Wells, G. B.; Kuo, L. C.; Makinen, M. W. In *Frontiers in Bioinorganic Chemistry*; Xavier, A. V., Ed.; VCH Verlagsgesellschaft: Weinheim, FRG, 1986; pp 562-570.

Polyhedral Clusters in Solids: The Electronic Structure of Pentlandite

Jeremy K. Burdett* and Gordon J. Miller

Contribution from the Department of Chemistry, The University of Chicago, Chicago, Illinois 60637. *Received September 15, 1986*

Abstract: The pentlandite structures are transition-metal sulfides that contain distinguishable metal atom cubes and exist only for certain combinations of the Fe group elements, Co_9S_8 being the only known binary phase. In this paper, we assemble the structure from the naked cube cluster after demonstrating the inadequacies of a ligand field analysis in rationalizing its physical properties. Molecular analogues also exist that exhibit different structural and physical features based upon the influence of a few orbitals near the HOMO-LUMO gap. We stress the importance of the octahedrally coordinated metals to the Co_8S_8 framework and how it contributes to the stability of Co_9S_8. Finally, the relative stabilities of various structural alternatives, both observed and hypothetical, for transition-metal sulfides of stoichiometry MS with tetrahedrally coordinated metal atoms are examined as a function of d-count by using the method of moments.

Transition-metal sulfides provide the crystal chemist a number of diverse structural types to study.[1] Many have no counterparts among the oxide compounds, e.g., the pyrites and marcasites, the NiAs structure, and the layered MoS_2, $CdCl_2$, and CdI_2 structure types. Like intermetallic compounds, their chemical formulas may not depict normal chemical valences, as in Co_9S_8, $Rh_{17}Se_{15}$, or N_3S_2. Such rather unique phases exhibit a variety of physical properties—metallic lustre, reflectivity, and electronic conductivity. The crystal structures of several transition-metal sulfides show close metal-metal distances, indicative of metal-metal bonding to some extent. These arise from the specific site occupations in the sulfide matrix or by distortions of an "ideal" high-symmetry arrangement of atoms to one of lower symmetry, e.g., the NiAs to MnP transition.

In this paper we shall examine the electronic properties of a class of sulfide compounds called π-phases or pentlandites,[2] with

(1) Comprehensive discussions of metal sulfides occur in the following: (a) Wuensch, B. J. In *Reviews in Mineralogy*; Ribbe, P., Ed.; Mineralogical Society of America: Washington, DC, 1982; Vol. 1, Sulfide Mineralogy. (b) Hulliger, F. *Struct. Bonding* **1968**, *4*, 83. (c) Jellinek, F. In *Inorganic Sulfur Chemistry*; Nickless, G., Ed.; Elsevier: Amsterdam; p 669. (d) Vaughan, D. J.; Craig, J. R. *Mineral Chemistry of Metal Sulfides*; Cambridge University Press: New York, 1978.

(2) (a) Knop, O.; Ibrahim, M. A. *Can. J. Chem.* **1961**, *39*, 297. (b) Knop, O. *Chem. Ind.* **1962**, 739.

0002-7863/87/1509-4081$01.50/0

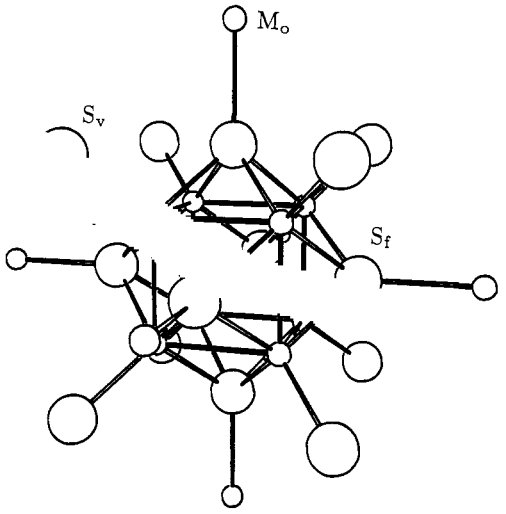

Figure 1. The cluster in pentlandite with its coordination environment, important distances, and angles. M_o, octahedral metals; M_t, tetrahedral metals; S_f, face-capping sulfurs; and S_v, linking sulfides.

stoichiometry M_9S_8, using Extended Hückel type band calculations. Their notable structural feature is a cubic cluster of metals within the sulfide matrix. These phases are naturally occurring materials, usually found with other sulfide minerals, e.g., pyrrhotite (Fe_7S_8), pyrite (FeS_2), and chalcopyrite ($CuFeS_2$).[3] All are metallic and exhibit a fairly narrow range of valence electron concentration, i.e., the number of electrons per unit cell volume. Using overlap and symmetry based arguments, we shall address the question of electron concentration, the stability of the cube cluster, and the general bonding properties of these sulfides.

The Structural Participants

The prototypic pentlandite is the synthetic material Co_9S_8, with space group $Fm3m$ and four formula units per unit cell.[4] Figure 1 illustrates the principal structural features, emphasizing the cubic cluster of metal atoms. There are two symmetry-inequivalent types of metal and sulfur atoms which produce the following descriptive formula, $Co[Co_8S_6]S_2$. The structure includes a nearly cubic-closest packing of sulfur atoms with transition metals occupying one-eighth of the octahedral and one-half of the tetrahedral interstices. The six coordinate metal atoms have site symmetry O_h, while the four coordinate metals are trigonally distorted, local symmetry C_{3v}, with one short and three longer metal–sulfur distances. The sulfur atoms also show two different coordination environments: (1) 75% have five metal neighbors arranged in a tetragonal pyramid—the four basal metals form one face of the cube; and (2) 25% are tetrahedrally coordinated by four metal atom cubes. Figure 1 indicates the various bond distances and angles found in Co_9S_8.

The natural pentlandites contain mixtures of Fe, Co, and Ni distributed throughout the metal sites.[5] The relative proportion of metal atoms, as determined from microprobe analysis, always provides an effective d-electron concentration per formula unit close to 65 (note that this value corresponds to that of $(Co_9)^{16+}$). In fact, of the three end members of the binary system, Fe_9S_8, Co_9S_8, and Ni_9S_8, only the cobalt sulfide forms a stable, homogeneous phase. A cubic iron sulfide, proposed to be isostructural to Co_9S_8 based upon similar X-ray diffraction patterns, was formed as a thin film by flash evaporation and vacuum deposition.[6] No single-crystal data, however, we ever published. More recently, Knop and co-workers synthesized a variety of tertiary and quaternary π-phases using Fe, Co, and Ni as well as Ru, Rh, and Pd.[7] Table I lists a number of pentlandites reported in the literature accompanied with their lattice constants, a_0. One quite notable feature is the substantial increase in a_0 with decreasing Co content: the isoelectronic Co_9S_8 and $Fe_{4.5}Ni_{4.5}S_8$ structures differ by 0.18 Å in their lattice constants! In the π-phase containing the heavier transition metals, Ru, Rh, Pd, and Ag, these atoms occupy the octahedral sites exclusively.[5,7] Due to the increased size of these heavier transition metals, the lattice constants are relatively larger than their first-row analogues. The common physical features of all pentlandites are their metallic and Pauli paramagnetic behavior as well as the indeterminate valency of the tetrahedrally coordinated metal atoms.

Cubic metal clusters with surrounding anions are not exclusive to the π-phases. Nevertheless, few other examples exist. Holm and co-workers recently synthesized and characterized $\{[Co_8(\mu_4\text{-}S)_6(SPh)_8]^{4-,5-}\}$, cluster anions that contain the Co_8S_6 rhombic dodecahedral unit found in Co_9S_8.[8] Crystallographically, these

Table I. The Pentlandites: Lattice Constants and d-Electron Concentrations

composition	a_0 (Å)	d electrons
Co_9S_8	9.9273	65
Co_8FeS_8	9.941	64
Co_8NiS_8	9.942	66
$Co_7Fe_2S_8$	9.951	63
Co_7FeNiS_8	9.952	65
$Co_6FeNi_2S_8$	9.967	66
$Co_5FeNi_3S_8$	9.983	67
$Co_4Fe_2Ni_3S_8$	9.995	66
$Co_4FeNi_4S_8$	10.000	68
$Co_3Fe_3Ni_3S_8$	10.010	65
$Co_3FeNi_5S_8$	10.021	69
$CoFe_4Ni_4S_8$	10.067	65
$Fe_5Ni_4S_8$	10.128	64
$Fe_{4.5}Ni_{4.5}S_8$	10.109	65
$Fe_4Ni_5S_8$	10.100	66
Co_8RuS_8	9.944	64
Co_8RhS_8	9.977	65
Co_8PdS_8	10.008	66
$Fe_4Ni_4RuS_8$	10.046	64
$Fe_4Ni_4RhS_8$	10.087	65
$Fe_4Ni_4PdS_8$	10.216	66
$Fe_4Ni_4AgS_8$	10.521	67

Table II. Geometrical Parameters of Cluster Compounds Containing the Rhombic Dodecahedral Unit

compound	d(M–M)[a]	d(M–X_f)[a]	d(M–X_t)[a]	ref
$Co_8S_6(SPh)_8^{4-}$	2.657	2.228	2.240	(71)
$Co_8S_6(SPh)_8^{5-}$	2.674	2.236	2.276	(72)
Co_9S_8	2.514	2.231	2.122	(70)
$Fe_{4.5}Ni_{4.5}S_8$	2.533	2.257	2.156	(68)
$Ni_8(CO)_8(PPh)_6$	2.648	2.183	1.78	(73)
$Ni_8(PPh)_6(PPh_3)_4$	2.53	2.14	2.26	(75)
$Ni_8S_6Cl_2(PPh_3)_6$	2.68	2.21	2.25 (Ni–P) 2.20 (Ni–Cl) 2.21 (Ni–S)	(76)
$Ni_8(PPh)_6Cl_4(PPh_3)_4$	2.61	2.21	2.24 (Ni–P) 2.24 (Ni–Cl)	(74)
$Ni_8(PPh)_6(CO)_4(PPh_3)_4$	2.67	2.20	2.27 (Ni–P) 1.80 (Ni–C)	(74)
$Fe_8S_6I_8^{3-}$	2.718	2.32		(77)
Bartonite	2.724	2.294	2.269	(79)
$K_6LiFe_{24}S_{26}Cl$	2.72	2.30	2.30	(78)

[a] All distances, in Å, represent average values. X_f are face-capping atoms and X_t are the terminal ligands

(3) Rajamani, V.; Prewitt, C. T. *Can. Miner.* **1973**, *12*, 178.
(4) (a) Geller, S. *Acta Crystallogr.* **1962**, *15*, 1195; (b) Rajamani, V.; Prewitt, C. T. *Can. Miner.* **1975**, *13*, 75.
(5) Hall, S. R.; Stewart, J. M. *Can. Miner.* **1973**, *12*, 169.
(6) Nakazawa, H.; Osaka, T.; Sakaguchi, K. *Nature Phys. Sci.* **1973**, *5*, 13.
(7) Knop, O.; Huang, C.-H.; Reid, K. I. G.; Carlow, J. S.; Woodhams, F. W. D. *J. Solid State Chem.* **1976**, *16*, 97.
(8) (a) Christou, C.; Hagen, K. S.; Holm, R. H. *J. Am. Chem. Soc.* **1982**, *104*, 1744. (b) Christou, C.; Hagen, K. S.; Bashkin, J. K.; Holm, R. H. *Inorg. Chem.* **1985**, *24*, 1010.

cubic fragments possess only inversion symmetry, yet in final refinements, they deviate only slightly from $m3m$ symmetry. As indicated in Table II the Co–Co distance in the Holm cluster is greater than the corresponding distance in Co_9S_8 by 0.16 Å. The face-capping sulfur atoms, however, have identical bond distances to the Co atoms in both structures. This cluster topology is found in several recent Ni analogues and one Fe cluster: the complete Ni prototype being $Ni_8(\mu_4'PC_6H_5)_6(CO)_8$ synthesized by Dahl and colleagues[9] while the Fe example is $[Fe_8S_6I_8]^{3-}$.[10] Table II lists the important geometrical parameters of these synthetic cluster compounds as well as those of Co_9S_8 and $Fe_{4.5}Ni_{4.5}S_8$ for comparison.

In the final set of examples, Fe_8S_6 units occupy sites of tetragonal point symmetry as opposed to the cubic pentlandites and are linked together via bridging sulfide groups. In the Djerfisherite-like compound,[11] $(K_6Cl)\{Li[(Fe_8S_6)S_{8/3}]_3\}$, the local symmetry of the cluster unit is D_{4h}. The peripheral sulfur atoms are three-coordinate to Fe: the missing vertex of tetrahedral coordination is directed toward a face of the K_6Cl octahedron. The other example is Bartonite, $(K_6Cl)_2\{[Fe_8S_6]S_{8/3}\}_6$, a structural isomer of Djerfisherite, in which two site symmetries of the cluster are found: D_{4h} and D_{2d}.[12] Table II also lists some relevent geometrical parameters for these materials.

A Ligand Field Analysis

For the series of pentlandite related materials, three major interatomic interactions influence the observed geometries: (1) the ligand field effects of the sulfur atom on the transition-metal orbitals; (2) metal–metal interactions within the cubic fragment; and (3) the matrix effect of the sulfur atoms. Previous descriptions of the electronic structure of pentlandite emphasized the ligand field interactions,[1d,13] producing the symmetry-induced d-level splitting into the σ nonbonding e levels and the σ^* type t_2 levels. These schemes introduced metal–metal bonding via the unpaired electrons in the t_2 orbitals, thus broadening these levels into bands, shown in **1**. Such analysis assumes the metal–metal interaction to be a perturbation on the ligand field splittings. Furthermore, upon dispersion of the molecular levels into bands, metal–metal bonding and antibonding levels should occur near the bottom and the top of each band, respectively. We shall investigate the adequacy of this model here.

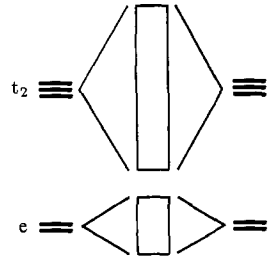

1

The cubic metal cluster arises from a condensation of eight tetrahedrally coordinated metal atoms. The symmetry imposes some severe restrictions on the distribution of energy levels and the strength of the metal–sulfur interactions. In Figure 2 we follow the d-orbital manifold for the system of two edge-sharing MS_4 tetrahedra as various interatomic forces are "turned on".[14] With only metal–sulfur interactions, the familiar two-below-three splitting per transition metal remains although it is not entirely e-below-t_2, a result of coupling through the bridging sulfur atoms.

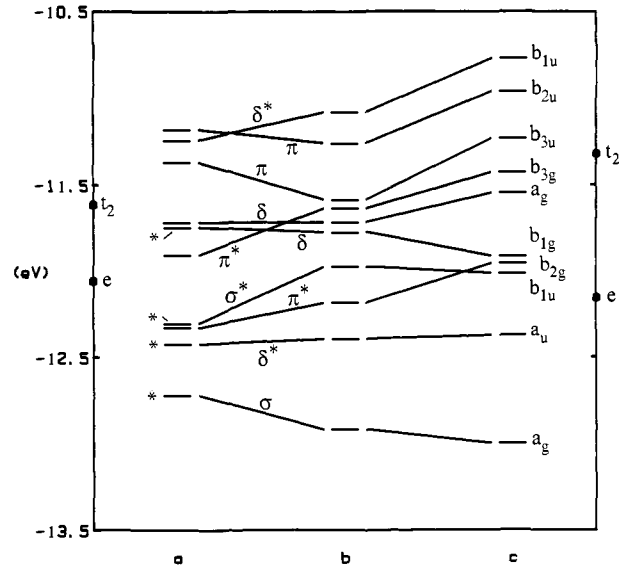

Figure 2. The d-orbital energy levels for the dimer M_2S_6. (a) Only M–S interactions; (b) M–S and M–M interactions; and (c) M–S, M–M, and S–S interactions. The irreducible representations are appropriate for D_{2h} point symmetry while σ, π, and δ indicate the type of M–M overlap. The d-orbital energies for the tetrahedral MS_4 complex are indicated with and without S–S interactions on the left and right, respectively. In part a, and asterisk labels those four levels derived from the e orbitals of MS_4.

Under D_{2h} point symmetry, the "e type" levels span the representations $a_g + b_{1u} + b_{1g} + a_u$, while the "$t_2$ type" levels span $a_g + b_{2g} + b_{3g} + b_{1u} + b_{2u} + b_{3u}$; all levels are nondegenerate. The e level (the b_{1g} orbital) occurring at −11.75 eV is destabilized due to an enhanced orbital contribution from the bridging sulfurs. Two t_2 levels are stabilized by a reduced interaction between the transition metal and the bridging sulfurs. The b_{2g} orbital at −12.32 eV contains a large component from the appropriate metal p orbitals which decreases the size of the overlap between the metal-centered and bridging sulfur orbitals. Also the b_{3g} orbital at −11.91 eV has no symmetry adapted orbital contribution from the bridging sulfurs, **2**.

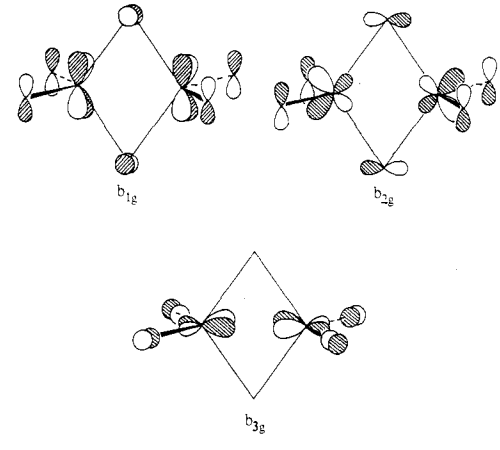

2

With all metal–metal overlap integrals set to zero, Figure 2a illustrates these through-bond coupling effects exclusively. Once we include the metal–metal interactions, the expected trends occur in the eigenvalue scheme: those levels which are metal–metal bonding are stabilized while the antibonding levels are destabilized. The d-band range widens by 0.3 eV with no major redistribution of levels especially concerning the metal–metal π and π^* orbitals, implying that through-bond coupling dominates. Can we gauge

(9) Ni clusters include the following: (a) Lower, L. D.; Dahl, L. F. *J. Am. Chem. Soc.* **1976**, *98*, 5046. (b) Fenske, D.; Basoglu, R.; Hachgenei, J.; Rogel, F. *Angew. Chem.* **1984**, *96*, 160. (c) Fenske, D.; Hachgenei, J.; Rogel, F. *Angew. Chem.* **1984**, *96*, 959. (d) Fenske, D.; Hachgenei, J.; Ohmer, J. *Angew. Chem.* **1985**, *97*, 684.

(10) The Fe cluster: Pohl, S.; Saak, W. *Angew. Chem.* **1984**, *96*, 886.

(11) Tani, B. *Am. Miner.* **1977**, *62*, 819.

(12) Evans, H. T.; Clark, J. R. *Am. Miner.* **1981**, *66*, 376.

(13) Prewitt, C. T.; Rajamani, V. In *Reviews in Mineralogy*; Ribbe, P., Ed.; Mineralogical Society of America: Washington, DC, 1982; Vol. 1, Sulfide Mineralogy.

(14) Summerville, R. H.; Hoffmann, R. *J. Am. Chem. Soc.* **1976**, *98*, 7240.

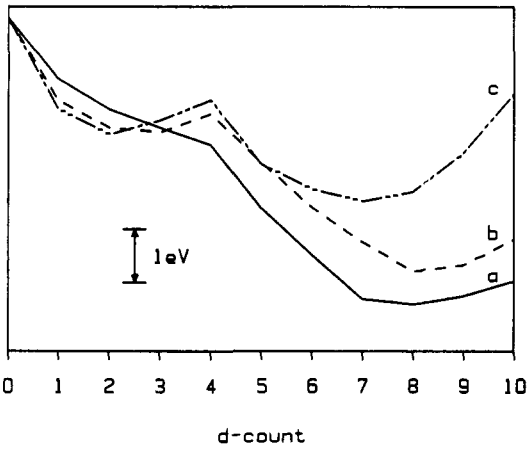

Figure 3. The total energy of the M_2S_6 dimer with respect to two isolated MS_4 fragments. The energy is calculated for the d-manifold only. Since the stoichiometry differs in the two cases, the energy zero is arbitrary. Lines a, b, and c correspond to Figure 2.

the role metal–metal bonding has on the stability properties of these condensed tetrahedra as a function of d-count? In Figure 3 we compare the total energy of the d-electron levels in M_2S_6 with two isolated MS_4 units for the various stages of included overlap integrals. The graph indicates that metal–metal interactions subtly influence the relative stability of these condensed systems for electron counts near d^4 and d^7–d^8 primarily through M–M π-bonding, although we find that through-bond coupling essentially dominates the features of curve b in Figure 3. Therefore, one should use caution when applying the arguments leading to scheme **1** since for cases in which a transition metal coordination sphere is shared among several metal centers, the effective ligand field will be severely altered.

Concerning the matrix effect of the anions, Figure 2c indicates that the d-manifold broadens by an additional 0.39 eV when sulfur–sulfur interactions are included. The greatest perturbations naturally occur with those levels containing an appreciable amount of sulfur character—the levels derived from the t_2 orbitals, all of which become destabilized. Furthermore, the energy difference curve in Figure 3c has a relative minimum at d^7 rather than at d^8 for the previous two cases. This shift arises from the significant σ^* interaction between the bridging sulfides in the b_{3u} orbital shown in **3**.

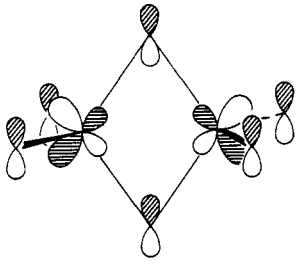

3

With these molecular considerations in mind, we illustrate the e and t_2 projections of the total density of states (DOS) for the tetrahedrally coordinated metals of Co_9S_8 in Figure 4. The diagrams indicate that these two sets of d levels are not clearly separated. We should point out, however, that the majority of the e projection occurs between −13.9 and −12.2 eV, including a fairly sharp band (width of 0.3 eV) at −13.7 eV. The t_2 projection is more dispersive, as expected, with significant components in the M–S bond and antibonding regions. As a result, a strict ligand field analysis does not illuminate the reasons for the narrow range of electron concentration observed for the pentlandites.

In contrast, the d orbitals of the octahedrally coordinated metals are well separated into t_{2g} and e_g bands, shown in Figure 5. The t_{2g} band is completely occupied for a calculated Fermi level at −11.49 eV for Co_9S_8. These six coordinate metals are critical to the stability of the pentlandites especially with regard to the nature

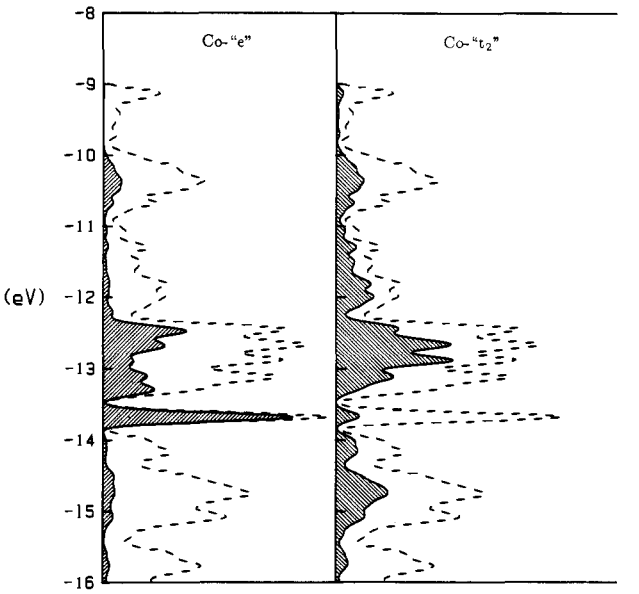

Figure 4. The e and t_2 projections of the tetrahedrally coordinated metals in Co_9S_8. The dashed curve represents the total DOS. Although not indicated, ϵ_F is −11.49 eV.

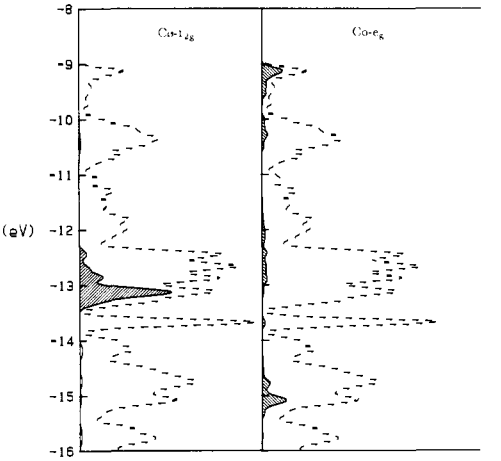

Figure 5. The t_{2g} and e_g projections for the octahedral metals of Co_9S_8. These projections are scaled by a factor of 2.0. The dashed curve is the total DOS.

of the mteal in the interstice, a point we shall discuss later in the discussion.

In the following sections we shall abandon the simple ligand field arguments and focus on the metal–metal interactions, the requirements of through-bond coupling with the bridging sulfides, as well as the sulfide matrix effects in the cluster. We shall produce the variety of observed structures by progressively considering the succession of ligand shells around the isolated metal cube.

The Rhombic Dodecahedron

Figure 6 illustrates the M_8S_6 fragment energy level diagram derived from the metal orbitals of the cube. The d-manifold of the metal cube cluster has a distinct gap of 0.3 eV, separating 29 levels from the 11 metal–metal antibonding levels. Occupation of all 29 bonding and nonbonding orbitals provides 58 metal-centered electrons, corresponding to $[(Co^{2+})_8]^{2-}$. How does this spectrum arise? In the usual manner of describing cluster molecular orbitals, we separate the basis set into radial and tangential components. Under the cubic point group O_h, the radial d_{z^2} orbitals span $a_{1g} + t_{1u} + t_{2g} + a_{2u}$ and the two sets of tangential orbitals each span $e_g + t_{1g} + t_{2g} + e_u + t_{1u} + t_{2u}$. Since a more convenient local coordinate system has axes parallel to the edges of the cube, we choose to lower the point symmetry to D_{4h}, thereby splitting

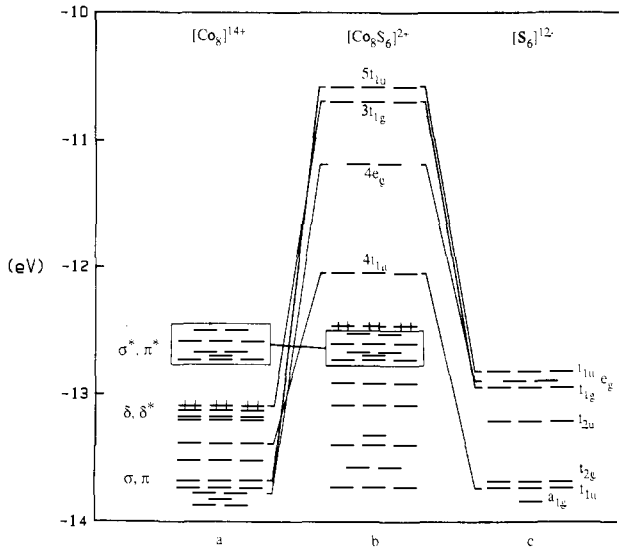

Figure 6. The molecular orbital interaction diagram between the M_8 cube and the S_6 octahedron to form the rhombic dodecahedral cluster M_8S_6. Only the M–S antibonding levels are labeled according to point group O_h. The primary M–M interactions are noted on the left. The HOMO for $[Co_8]^{14+}$ and $Co_8S_6^{2+}$ are indicated.

all degeneracies and eliminating various symmetry imposed orbital mixings. The energy levels for the d-manifold are easily constructed by forming symmetric and antisymmetric combinations of the d-orbitals for two M_4 squares. In the square the d_{xy}, d_{xz}, and d_{yz} orbitals from three mutually exclusive sets whereas the d_{z^2} and $d_{x^2-y^2}$ levels must be considered together. The radial components occur within proper linear combinations of the d_{xy}, d_{xz}, and d_{yz} orbitals at each site, viz., $(1/\sqrt{3})(\pm d_{xy} + d_{xz} + d_{yz})$. The interaction integral between these orbitals on two adjacent sites is

$$\beta_{rad} = \langle \Psi_{rad_1} | H | \Psi_{rad_2} \rangle = 0.67\beta_\pi + 0.33\beta_\delta$$

in which Ψ_{rad_i} indicates a radial orbital at site i, β_π and β_δ being the pure $d\pi$–$d\pi$ and $d\delta$–$d\delta$ interactions. Simple nodal plane analysis then predicts the splitting pattern shown in Figure 7a for the radial orbitals with nondegenerate levels at $\pm 3\beta_{rad}$ and triply degenerate levels at $\pm\beta_{rad}$ (Note: in the figure we resurrect the full cubic symmetry of the cube). The schematic diagrams for the two "tangential" sets—the ($d_{x^2-y^2}$, d_{z^2}) and the remaining (d_{xy}, d_{xz}, d_{yz}) sets—are shown in Figure 7, parts b and c. These were determined with use of the angular overlap model and the compatability relations between D_{4h} and O_h:

O_h		D_{4h}	O_h		D_{4h}
a_{1g}	↔	a_{1g}	a_{2u}	↔	b_{1u}
e_g	↔	$a_{1g} + b_{1g}$	e_u	↔	$a_{1u} + b_{1u}$
t_{1g}	↔	$a_{2g} + e_g$	t_{1u}	↔	$a_{2u} + e_u$
t_{2g}	↔	$b_{2g} + e_g$	t_{2u}	↔	$b_{2u} + e_u$

Combining these three MO diagrams into one energy level scheme produces the essential features of Figure 6a. When the symmetry-allowed orbital mixings are included, levels spanning similar irreducible representations will repel each other. The important participants are the t_{2g} levels just above the energy zero (in Figure 7). The three-orbital interaction opens a major gap by stabilizing the radial t_{2g} level, thereby separating eleven M–M d-antibonding levels from the remainder. However, these antibonding orbitals are destabilized to a limited extent by hybridization with appropriate symmetry adapted combinations of s and p orbitals. Before we introduce the face-capping sulfur atoms, using metal–metal bonding arguments exclusively suggests that a d-electron concentration of 58 electrons per M_8 unit will optimize the stability of the cube cluster.

For the rhombic dodecahedral cluster fragment, M_8S_6, we again observe the importance of through-bond coupling in transition-metal sulfides. When the six sulfur atoms interact with the metal

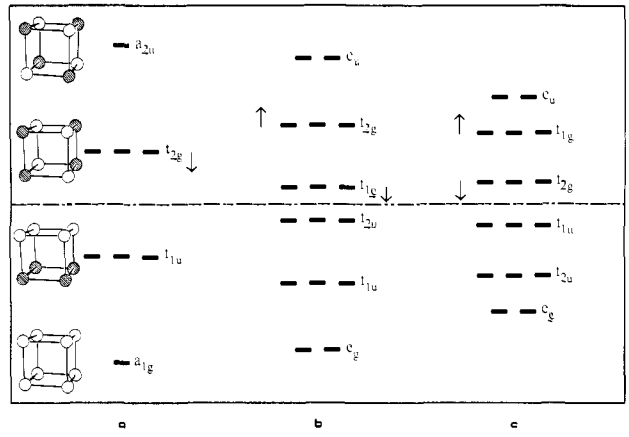

Figure 7. The energy spectrum for the d-orbitals of the cube predicted from the interaction of two M_4 squares. Parts a and b arise from the set (d_{xy}, d_{xz}, d_{yz}) and part c from the set ($d_{x^2-y^2}$, d_{z^2}): (a) the radial orbitals with their relevent phases shown to the left; (b) one tangential set involved in π and δ interactions; and (c) the tangential set with M–M σ and δ overlap. When interactions between the two sets are activated, the levels which strongly repel each other are marked by arrows.

cube, the eleven metal–metal antibonding orbitals remain largely unperturbed with use of only symmetry arguments. The sulfur p orbitals when separated into radial and tangential components transform as $a_{1g} + t_{1u} + e_g$ (radial) and $t_{1g} + t_{2g} + t_{1u} + t_{2u}$ (tangential). Five of the mteal–metal antibonding levels match none of the symmetry-adapted combinations of sulfur orbitals, so they are not affected. The remaining six M_8 antibonding orbitals either overlap poorly with the face-capping sulfides or have significant Co 4s and 4p components so that all 11 metal–metal antibonding levels are found in the set of occupied orbitals for M_8S_6 for all geometries near those observed and for a variety of transition-metal parameters. This certainly suggests that metal–metal bond strengths are not maximized in these structures.

What controls the observed splitting pattern? Our calculations reveal that the largest gap occurs between the $4t_{1u}$ orbital at −12 eV and the e_g level at −11 eV. Another smaller gap of 0.4 eV is found between the same $4t_{1u}$ level and the orbital below. We cannot absolutely assign the levels below $4t_{1u}$ because of subtle energy shifts as we change internuclear distances, although this range maintains its general orbital characteristics. The energetic pattern of the eleven levels above the HOMO for $(Co_8S_6)^{2+}$, however, remains unchanged for feasible geometrical or atomic modifications. Alongside the M_8S_6 fragment spectrum in Figure 6b we indicate the symmetry-adapted orbitals of the S_6 octahedron. Within the 3p levels the spectrum is simply seven bonding ($a_{1g} + t_{1u} + t_{2g}$), three nonbonding (t_{2u}), and eight antibonding ($t_{1g} + e_g + t_{1u}$) levels. These eight antibonding sulfur levels form a considerable component of the eight orbitals of M_8S_6 in the range −11.0 to −10.5 eV. Three typical examples of these matrix orbitals are shown in **4**, **5**, and **6**. From their nodal character we see that

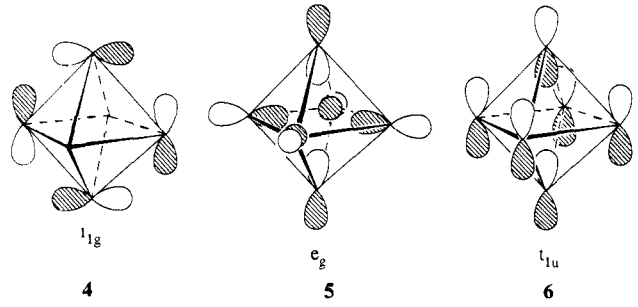

4 **5** **6**

the metal d orbitals of the cube best suited for strong interaction with the ligands should contain some bonding character. The $4t_{1u}$ level, the LUMO for $(Co_8S_6)^{2+}$, arises from the destabilizing interaction between the bonding t_{1u} matrix orbital and a t_{1u} radial-type metal level. This orbital remains rather close to the occupied levels as a result of a significantly stabilizing Co-4s

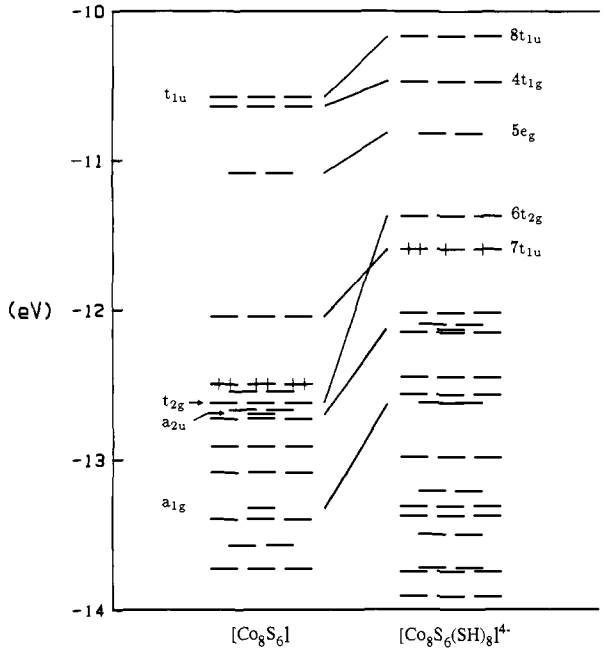

Figure 8. The energy level diagram for $Co_8S_6(SH)_8$ derived from that of M_8S_6 in Figure 6. We maintained O_h symmetry by keeping the Co–S–H angle at 180°. The radial M_8S_6 levels are indicated. The HOMO is the incompletely occupied $7t_{1u}$ level.

component. Thus, the optimal electron count for this fragment is 106 electrons, corresponding to 58 electrons per M_8 group. This concentration equals that obtained by using the metal–metal bonding arguments, but the reasoning has now changed. The through-bond coupling and matrix effects of the sulfur atoms are quite influential in controlling the electronic structure.

Capping the Cluster

Since we can understand the d-electron concentration in these cube clusters from the analysis of the M_8S_6 fragment, we expect that completing the coordination environment of the metal atoms should produce rather minor changes in the global stability effects. That is, the M–S antibonding levels in the M_8S_6 unit will remain unoccupied when "capped" so as to preserve the integrity of this fragment. Figure 8 illustrates how the orbitals of the Co_8S_6 fragment interact with the orbitals of an $(SH)_8$ unit in order to produce the electronic environment in the known cluster $[Co_8S_6(SPh)_8]^{4-}$. We selected the SH bonds to lie parallel to the threefold axis of the cube although in the observed compound the Co–S–Ph angle is nonlinear. The results of a calculation with SH units at an angle of 109.5° do not change the interpretation but simply reduce the degeneracies of many of the levels. The radial metal orbitals in M_8S_6, labeled in the figure, show strongest interaction with the donor ligands, being destabilized on average by ~1.2 eV. The important levels to consider are $6t_{2g}$ and $7t_{1u}$; an example of each is shown in **7**.

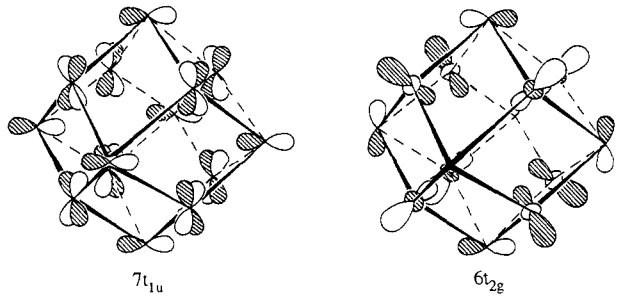

7

The radial $6t_{2g}$ orbital is directed toward each SH ligand providing strong overlap with an sp-hybrid orbital on sulfur, whereas the $7t_{1u}$ orbital is mostly "tangential" in its metal d-

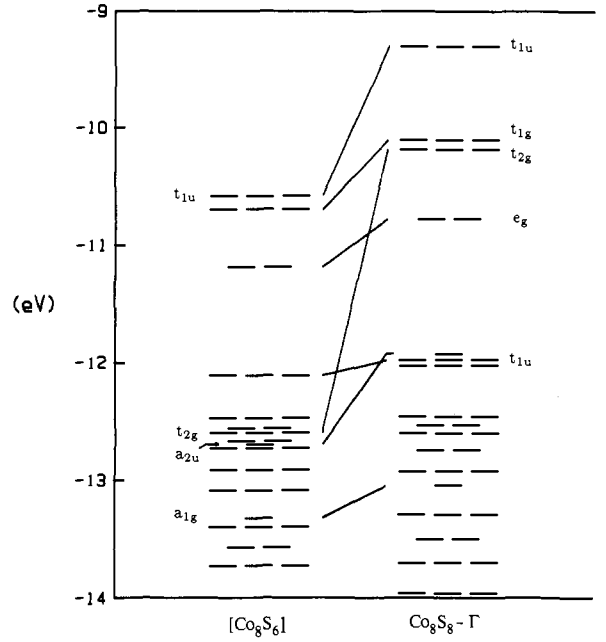

Figure 9. The energy spectrum for Co_8S_8 at Γ derived from the M_8S_6 fragment. Note the position of the t_{2g} level as compared to Figure 8.

component and has a greater energy separation from the sulfur sp-hybrid. All of these conditions contribute to the destabilization of the $6t_{2g}$ level above $7t_{1u}$, although their energy separation is only ~0.2 eV. Filling the molecular levels in the aufbau sense, we find that the $7t_{1u}$ orbital is two-thirds occupied. Since we suggested that $(Co_8S_6)^{2+}$ represented a closed-shell system, the partial occupancy of this triply degenerate level is consistent with the assignment $(Co_8S_6)^{4+}$, as mentioned by Christou et al.[8b] The one-electron reduction of the cluster anion leaves one unpaired electron which agrees with the observed magnetic susceptibility at 6 K of 1.95 μ_B (indicating an $S = {}^1/_2$ ground state). However, concerning the $[Co_8S_6(SPh)_8]^{4-}$ cluster, our one-electron theory is unable to adequately examine the exchange and correlation effects that contribute to its magnetic properties. Since the "unoccupied" $6t_{2g}$ level is energetically close to the occupied levels, we anticipate the spin-pairing energy to be relieved by partial occupation of this orbital.

A three-dimensional analogue to these cluster anions is the hypothetical structure of a defect pentlandite, Co_8S_8, in which the octahedrally coordinated metal atoms have been removed. The sulfide groups are not only electron donors to the fundamental cluster Co_8S_6, as in the previous example, but also serve to link together four of these units. The requirements of translational symmetry, however, produce an interaction scheme which is rather different from the spectrum for the $[Co_8S_6(SH)_8]^{4-}$ cluster, as shown in Figure 9. From the energy levels for Co_8S_8 at Γ, the zone center, we find that the $6t_{2g}$ level of the cluster anion (now labeled simply t_{2g} for the solid) lies at a higher energy in the solid, so that there are now eleven rather than eight conspicuous metal–sulfur antibonding levels. A considerable gap, 1.27 eV, occurs which produces an optimal electron count appropriate for $[Co_8S_8]^{2-}$. Again, we predict a preferred electron concentration per M_8 group at 58 electrons.

How have the orbital interactions been modified in the solid? Certainly, the level of interest is "$6t_{2g}$". At the zone center, the point symmetry of the tetrahedral sulfides is T_d so that their s and p orbitals transform as a_1 and t_2, respectively. The Bloch orbital involving the radial t_{2g} level of the Co_8S_6 fragment transforms as t_{1u} at the sulfide positions, shown in **8**. This level is significantly destabilized due to both the relatively small energy separation (~0.6 eV) between the Co_8S_6 t_{2g} orbital and the sulfur p orbital as well as their significant orbital overlap. In the cluster anion, $[Co_8S_6(SH)_8]^{4-}$, the energy difference between the radial t_{2g} level for Co_8S_6 and the relevent phenyl sulfide "p" orbital has increased to 3.0 eV while the overlap integral has increased. The

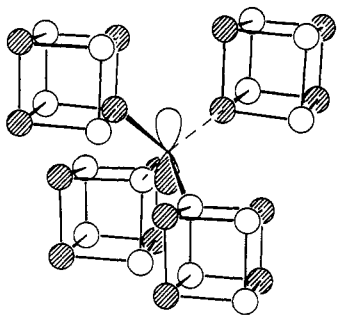

8

increased energy separation dominates and results in a smaller interaction with the t_{2g} level. In **9** we show the changes that occur

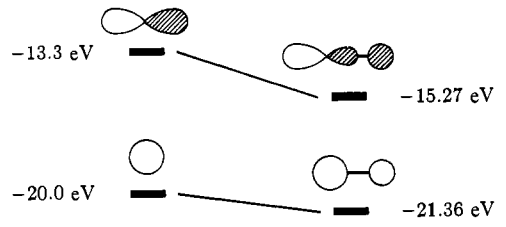

9

in the sulfide ligands when going from the solid to the cluster. The sulfur p_σ orbital is stabilized by the bonding interaction with the phenyl group (in our case, H) and contains a contribution from the s 3s orbital, increasing the orbital density toward the metal atom. On the other hand, the Co_8S_6 t_{1u} level at −12.1 eV is destabilized to a smaller extent in the solid arising solely from a reduced angular overlap. The energy difference in the two cases is nullified because the hydrogen 1s orbital cannot perturb the sulfur $p\pi$ orbitals.

Is the story thus far presented any different when π-acceptors are used as terminal ligands rather than π-donors, like sulfur or the halogens? Figure 10 illustrates the interaction diagram for $Ni_8(PH)_6(CO)_8$ as assembled from the rhombic dodecahedral $Ni_8(PH)_6$ cluster with eight CO groups. Though the level structure for $Ni_8(PH)_6$ and Co_8S_6 is similar in many aspects, we point out the large separation (1.2 eV) between the $4e_g$ and the $5t_{1u}$ orbitals in the Ni cluster. Since $Ni_8(PH)_6$ requires 116 electrons, 10 greater than for $Co_8S_6^{2+}$, all levels through $4e_g$, inclusive, are compeltely occupied. When the metal–carbon interactions are turned on, we observe both the σ-donating and the π-accepting nature of the carbonyl ligands. The $4e_g$ orbital is stabilized by ~0.3 eV via a strong Ni–C π interaction. Since the $4t_{2g}$ orbital is directed radially toward the carbonyl groups, this interacts with the CO σ_p orbitals, becoming the HOMO in $Ni_8(PH)_6(CO)_8$. With 120 cluster valence electrons, both $Ni_8(PPh)_6(CO)_8$ and $Ni_8(PPh)_6(PPh_3)_4(CO)_4$ are diamagnetic, in agreement with our prediction. Furthermore, Fenske and colleagues determined that $Ni_8Cl_4(PPh)_6(PPh_3)_4$ (116 cluster valence electrons) is paramagnetic with magnetic susceptibility data consistent with antiferromagnetic behavior.[9] Since PPh_3 is a good σ-donor ligand and Cl is a weaker π-donor than S, we anticipate that the $4t_{2g}$ orbital will be the incompletely filled HOMO for this cluster as well.

Clearly, the number of valence electrons that maximizes the cluster stability depends upon the ligand system. For π-donors, lower electron concentrations (~110 electrons) are preferred whereas for π-acceptors a value of 120 electrons per cluster, as predicted by Lauher,[15] is optimal. From the energy level diagrams, the position of the $4t_{2g}$ level was crucial in determining these values. Although Extended Hückel theory is generally unreliable in predicting internuclear separations via optimization of the total energy, we can predict the trends in metal–metal bond distances by examining the occupancy of the $4t_{2g}$ orbital as well as compare

(15) Lauher, J. W. *J. Am. Chem. Soc.* **1978**, *100*, 5305.

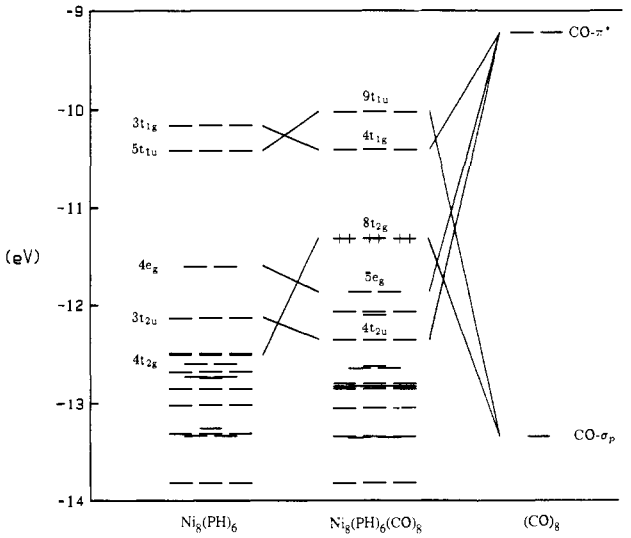

Figure 10. The interaction diagram between $Ni_8(PH)_6$ and $(CO)_8$ to form the molecule $Ni_8(PH)_6(CO)_8$. Only the CO σ_p- and π^*-levels fall within the energy range. The HOMO is the $8t_{2g}$ level.

Table III. Metal–Metal Overlap Populations and $4t_{2g}$ Occupancy for Pentlandite-Type Compounds

compound	d(M–M) (Å)	overlap pop.	t_{2g} occup.
Co_9S_8	2.514	0.070[a,b]	0
$Co_8S_6(SPh)_8^{4-}$	2.657	0.064[a]	$0 < x < 3$
$Co_8S_6(SPh)_8^{5-}$	2.674	0.061[a]	$0 < x < 3$
$Ni_8(PPh)_6(PPh_3)_4$	2.53	0.069[c]	0
$Ni_8(PPh)_6Cl_4(PPh_3)_4$	2.61	0.063[c]	2
$Ni_8(PPh_3)_6Cl_2S_2$	2.67	0.057[c]	4
$Ni_8(PPh)_6(CO)_8$	2.648	0.051[c]	6
$Ni_8(PPh)_6(CO)_4(PPh_3)_4$	2.67	0.051[c]	6

[a] Calculated for d(M–M) = 2.543 Å, using Co parameters. [b] Calculated for Co_8S_8 network. [c] Calculated for d(M–M) = 2.62 Å, using Ni parameters.

the overlap populations in systems in which the distances are set equal. Table III lists some of the examples with their metal–metal distances, computed M–M overlap populations, and the t_{2g} occupation number (for the solid state cases, we list the occupancy at Γ). Recall that this t_{2g} orbital is one of the radial metal–metal antibonding levels of the cube, so that as its occupation increases, the M–M bond distance should increase as well. The results in Table III bear our this correlation reasonably well.

Metal–Metal vs. Metal–Sulfur Bonding

We noted previously that the strength of the M–M interaction is not maximized in these materials. The COOP (Crystal Orbital Overlap Population) curve for pentlandite certainly corroborates this statement (see Figure 11) since the Fermi levels for the range of observed electron counts lie in a rather weak M–M antibonding region. We can account for the features in the M–M COOP curve by examining the orbitals of the Co_8 cube using the local coordinate system in which the Cartesian axes are parallel to the edges of the cube. The d_{z^2} and $d_{x^2-y^2}$ orbitals are involved in σ and δ interactions while d_{xy}, d_{xz}, and d_{yz} participate in π and δ overlap. Figure 12 shows the projections of those bands which are predominantly σ, σ^*, π, and π^* between metal atom orbitals. The major contribution to the negative overlap population in the energy ranges −12.9 to −12.3 eV and −10.7 to −9.9 eV is the σ^* band. The π and π^* bands are energetically wider due to the increased overlap with the terminal sulfides. Note that the M–M π-bonding levels extend to higher energies than the π^* bands: a picture rather similar to the M_2S_6 dimer levels of Figure 2. Also, though not explicitly shown in the fragment orbital projections of Figure 12, the large metal–metal antibonding contribution above ϵ_F results from the mixing of Co 4s and 4p components in this region.

These arguments indicate that lowering the electron count per M_8 group from 58 depletes density from the σ-bonding levels whereas increasing the count soon populates M–M σ^* bands. Do

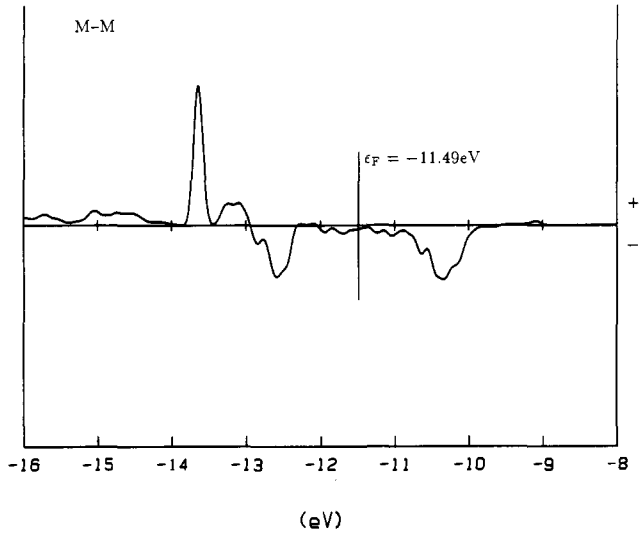

Figure 11. The M–M crystal orbital overlap population (COOP) curve for Co_9S_8: + indicates bonding, – indicates antibonding levels.

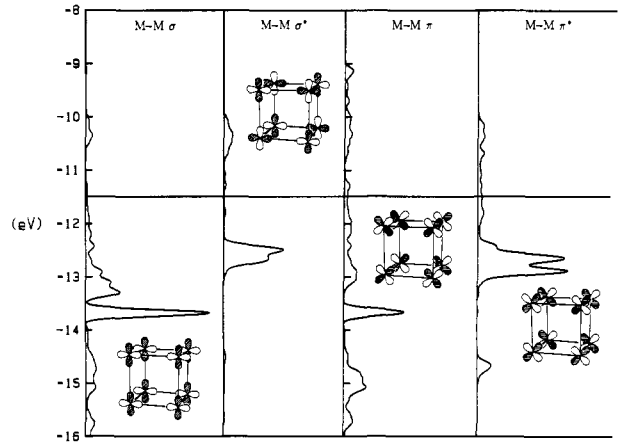

Figure 12. An M_8 fragment decomposition of the total DOS of Co_9S_8. The projections are labeled according to the principal M–M overlap shown. The line occurs at the Fermi level for Co_9S_8, –11.49 eV.

M–S interactions parallel the trends predicted by M–M bonding arguments only? From the COOP curves for the two types of M_{tet}–S linkages shown in Figure 13, we see that a similar upper bound for electron count occurs. By using a rigid band model, the Fermi levels for some observed pentlandites separate the bonding from the antibonding regions in the M_{tet}–S_v curve, although the entire region has rather small overlap populations. Also, strongly antibonding M_{tet}–S_f levels are kept unoccupied at these counts. The difference in magnitudes of the overlap populations for these two bond types again arises from Co s and p hybridization into the d manifold. Those orbitals which most effectively mix are the radial orbitals on the metal. The integrated populations for the M_{tet}–S_v (0.504) and M_{tet}–S_f (0.413) distances set equal agree with the sense of distortion at the tetrahedral metals. Therefore, the Fermi level is largely controlled by the M–S interactions with M–M σ-bonding setting a lower bound.

The Octahedral Metals

As suggested from the energy spectrum of Co_8S_8 at Γ, the metal–sulfur network needs two additional electrons in order to completely fill all orbitals below the major gap. The eleven bands left unoccupied are primarily M–S antibonding within the Co_8S_6 cluster. Two electron donor candidates include the alkaline-earths and a large number of the transition metals, yet, of the currently characterized pentlandites, only Fe, Co, Ni, Ru, Rh, Pd, and Ag are known to occupy the octahedral sites. These metal atoms are more electronegative and also smaller than their earlier counterparts in the periodic table. With the radius of the octahedral hole in the Co_8S_8 network being no larger than $\sim$1.25 Å, the

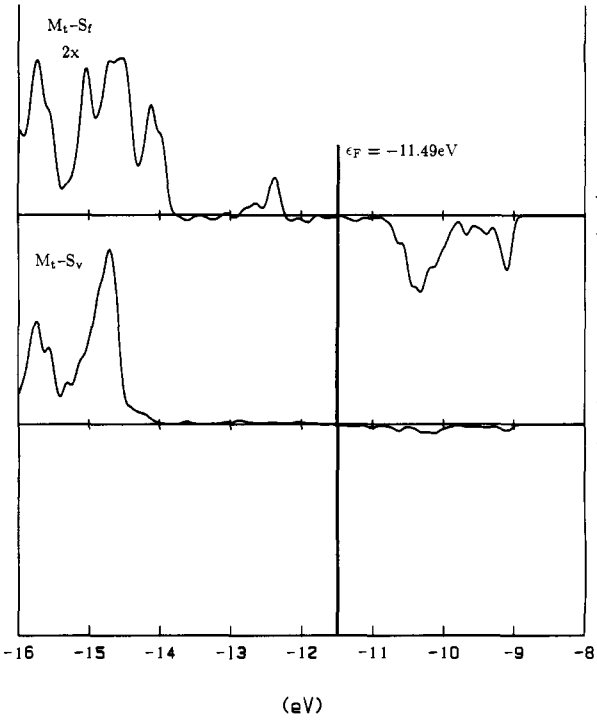

Figure 13. The M–S COOP curves for the two types of interactions between the four-coordinate metals in pentlandite. The atom symbols are the same as in Figure 1. The M_t–S_f curve is scaled by 2.0. The +/– convention is the same as in Figure 11.

alkaline-earth atoms Ca, Sr, and Ba cannot occupy these interstices due to size effects (Note: M–S distances in CaS, SrS, and BaS are 2.8418, 3.0040, and 3.184 Å, respectively).[16] However, Mg may certainly occupy the sites as the Mg–S distance is 2.595 Å in MgS.[16] The compound $MgCo_8S_8$ should not exhibit significant changes in conductivity from other pentlandites but may certainly show bond length differences. We shall elaborate on this point in the following discussion.

Concerning the transition-metal possibilities, we note that all known examples have completely occupied t_{2g} orbitals. Being σ-nonbonding levels, we infer that their d-orbital energies lie below the Fermi level for Co_8S_8. The earlier transition metals are more electropositive and, therefore, have higher d-orbital energies than the Fe-group metals. If these energies lie above the Co_8S_8 Fermi level, then the octahedral metal will donate more than two electrons to the sulfide network in order to achieve a constant chemical potential. These additional electrons occupy M–S antibonding bands which will destabilize the structure. Furthermore, the Fermi level will rise considerably above that for Co_8S_8 in order to accommodate the extra t_{2g} electrons.

To understand the effect of these interstitial metals, let us examine the nature of the orbital interactions in Co_8S_8 near its Fermi level. Figure 14 illustrates the energy bands for Co_8S_8 along two high-symmetry directions in the first Brillouin zone, ΓL and ΓX, respectively. From the connectivity within the M–S framework, the interactions between the M_8S_6 clusters and the linking sulfide groups control the dispersion of these bands. Under C_{3v} symmetry of ΓL, these sulfide p orbitals transform as a_1 + e. Therefore, for all points except Γ, the sulfur s and the a_1–p orbital are allowed to mix. This sulfide p orbital is directed toward a metal atom of the cube, which enhances its σ interaction but reduces its overlap with the remaining three clusters. Since the M–S antibonding levels at Γ, except the e_g orbital, contain only p-orbital contributions from the linking sulfides, this s–p hybridization stabilizes the nondegenerate bands. Their corresponding e bands, however, have no sulfur s character and so move to lower energies simply due to a diminished d–s overlap. The

(16) Pearson, W. B. *A Handbook of Lattide Spacings and Structures of Metals and Alloys*; Pergamon Press: New York, 1958.

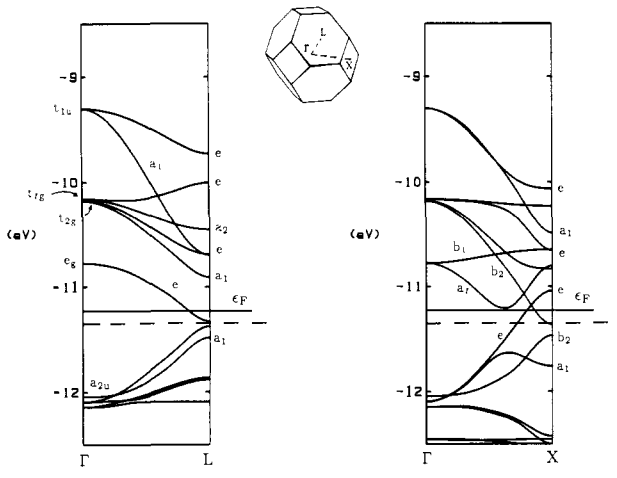

Figure 14. The energy bands for Co_8S_8 along ΓL and ΓX. The bands are assigned according to the groups C_{3v} and C_{4v}, respectively. ϵ_F for $Co_8S_8^{2-}$ is marked at −11.23 eV while the dashed lines indicate ϵ_F for Co_8S_8 at −11.34 eV.

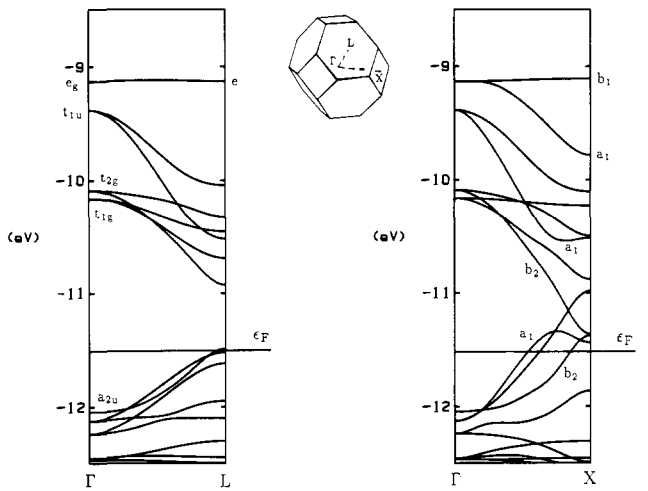

Figure 15. The energy bands for Co_9S_8 along ΓL and ΓL. The Fermi level, ϵ_F, equals −11.49 eV.

stabilization of the e_g level is more subtle. At Γ these levels have no component from the linking sulfides, a consequence of the transitional symmetry. Therefore, as we proceed away from Γ, this band should be destabilized by introducing a sulfur p-orbital component. In fact, through substantial mixing with the "t_{1g}" and "t_{2g}" bands, an avoided crossing occurs and this e band changes its orbital character. An important feature of this level crossing involves a switch in the metal–metal overlap population from positive (bonding) at Γ to negative (antibonding) at L. On the other hand, the occupied levels near ϵ_F, which have s-orbital components from the linking sulfides at Γ, now become destabilized due to the sp hybridization along ΓL. For example, the coordination shell of the terminal sulfide of the Γ-a_{2u} and L-a_1 levels is shown in **10**, indicating that the pure s component at Γ becomes an sp hybrid at L.

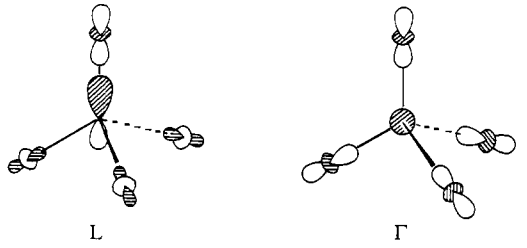

10

Similar arguments apply for the bands along ΓX which are classified under the group isomorphous to C_{4v}. The partially occupied metal–sulfur antibonding band is b_2 arising from the t_{2g} level at Γ. **11** shows how the orbital phases imposed by transitional

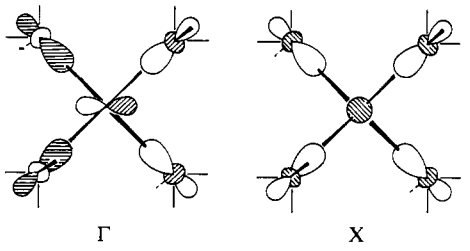

11

symmetry at X account for its dispersion. As in **11**, we only illustrate the sulfide coordination but recall the Γ-t_{2g} orbital shown in **8**. As opposed to the ΓL direction, the e_g level now splits into a_1 and b_1. The totally symmetry band and the occupied a_1 band from the t_{2u} orbital interact and undergo an avoided crossing in this direction so that at X these two a_1 bands switched character. In effect, for electron counts appropriate for $Co_8S_8^{2-}$, some M–S antibonding levels are now occupied.

Figure 14 also indicates the Fermi level for the neutral species Co_8S_8. Although this structure type is a plausible alternative for this stoichiometry, the band structure suggests that this framework would be stabilized by interstitial atoms which provide strong orbital interactions with the bands near ϵ_F. We show how these bands are affected by such Co atoms using similar band structure plots for Co_9S_8 in Figure 15. At Γ the site symmetry of these metal atoms remains O_h. The d manifold, therefore, separates into t_{2g} and e_g sets (recall Figure 5). Clearly, the e_g levels of the metal interact quite strongly with the e_g band of Co_8S_8. From Figure 6 this particular level is metal–metal bonding within the cube. In effect, the bonding M_{oct}–S_f e_g orbital also strengthens the M_{tet}–M_{tet} interaction, as indicated by an increase in the M_{tet}–M_{tet} overlap population from $Co_8S_8^{2-}$ (0.0764) to Co_9S_8 (0.0877). The M_{oct} t_{2g} set only weakly overlaps with the predominantly radial t_{2g} orbital of the Co_8S_6 fragment (**7**). The net result is that a sizable gap opens at L (0.55 eV) and the M_{tet}–S antibonding levels at X are destabilized to energies above ϵ_F. The dispersion characteristics of these bands remain identical with the corresponding bands in Co_8S_8.

If an alkaline-earth element occupies these voids, there are no d functions energetically accessible to interact with the Co_8S_8 framework. The bands for Co_8S_8 in Figure 14 would become a more appropriate description of $MgCo_8S_8$. As a consequence of the previous discussion, we anticipate longer M_{tet}–S and M_{tet}–M_{tet} distances in $MgCo_8S_8$ than in MCo_8S_8, where M is any late transition metal. Also, there is greater stability associated with the d-orbital contributions from the interstitial transition metals for not only is the e_g band removed from energies near ϵ_F but also the occupied t_{2g} orbitals of the octahedral metal serve to lower the Fermi level, thereby increasing the chemical potential.

Energetic Comparisons

We previously described the hypothetical sulfide structure in which the octahedrally coordinated metal atoms were removed. A solid with stoichiometry MS remains. There clearly exist an infinite number of possible structures having 50% tetrahedral hole occupancy in a ccp arrangement of anions. Three examples are shown in **12**, **13**, and **14**. **12** depicts the unit cell of sphalerite in which all metal–metal separations are maximized and both metal and sulfur atoms are tetrahedrally coordinated. The only binary transition-metal sulfides known are MnS (high-spin d^5 Mn^{II}), ZnS, and CdS (d^{10} M^{II}).[17] As expected, these compounds are semiconductors, MnS being antiferromagnetic as well. **13** represents a part of the layered structure mackinawite, FeS_{1-x}.[18,19] Every

(17) Wells, A. F. *Structural Inorganic Chemistry*, 5th ed.; Clarendon Press: Oxford, 1984.
(18) Vaughan, D. J.; Ridout, M. S. *J. Inorg. Nucl. Chem.* **1971**, *33*, 741.
(19) (a) Bertaut, E. F.; Burlet, P.; Chappert, J. *Solid State Commun.* **1965**, *3*, 335. (b) Goodenough, J. B. *Mater Res. Bull.* **1978**, *13*, 1305.

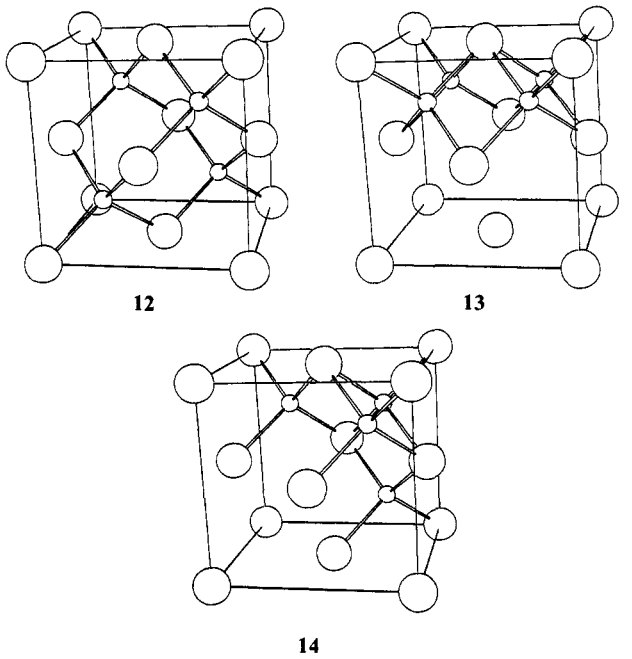

sulfide is coordinated to a square of metal atoms to form a tetragonal pyramid. Each Fe atom has four close metal–metal contacts. **14** illustrates another hypothetical distribution of cations for a binary sulfide. This local fragment is observed for ternary sulfides, e.g., the cubic structure of sulvanite, Cu_3VS_4.[20] The sulfur coordination is described as an "inverted tetrahedron".

We illustrate how the total energy of the defect pentlandite and these structural alternatives compares to that of sphalerite as a function of d count in Figure 16. Though the sphalerite structure is favored for all counts, we note certain relative minima in each curve. The preference for tetrahedral coordination at the anion dominates the effects of metal–metal bonding. As Table IV shows, we can mimic the structural energy ordering at d^0 by summing the fragment energies of the contributing M_4S species with 8 electrons. Eliminating this d^0 contribution, we can examine the energetic preferences due to metal–metal interactions. In agreement with experiment, these curves predict mackinawite to be favored at d^6 and pseudo-pentlandite at d^7. Though the energy differences are rather small, we emphasize the trends of these curves.

Application of the moments method[21] can help explain the features of these energy difference curves. We need to confine our attention to the metal d-levels exclusively. Although our previous discussion suggested that a strict "e-t_2" splitting in the condensed tetrahedral geometries may not be accurate, we shall now consider these two sets separately. The close metal–metal contacts in the sphalerite alternatives lead to immediate differences in the second moment involving metal–metal interactions. These second moment effects are observed in the ranges d^-d^4 and d^4–d^{10}. By selecting an appropriate coordinate system, the first range includes σ bonding while the second range contains π and δ interactions. Since the structures of interest are observed for d^6–d^8 metals, we shall only consider these electron counts. Table V lists the expressions for the second and fourth moments, μ_2 and μ_4, in terms of β_π and β_δ, the resonance integrals for π and ζ overlap between metals. Since $\beta_\pi > \beta_\delta$ in general, the expressions for μ_4 decrease in the order mackinawite > "sulvanite" > Co_8S_8. Therefore, the Co_8S_8 framework is expected to be electronically favored at the half-filled point, corresponding to d^7. At earlier counts, the larger second moment for mackinawite contributes to its stability. Finally, the binary sulvanite structure would not be favored at any point due to its intermediate fourth moment and a second moment equal to that for Co_8S_8. We note, however, that tertiary examples exist, e.g., Cu_3VS_4, in which the average d count per metal atom is 7.5.

What makes the pentlandite structure so energetically favorable for compounds in the region of Co_9S_8? From our previous discussion, we see that the cubic cluster is a feasible arrangement of transition metals when the d-electron concentration is 58 electrons, placing the metal atom in the Co group. Furthermore, though the quantitative accuracy of Extended Hückel results is generally unreliable, they do predict the Co_8S_8 framework to be preferred over the other metal sulfide networks with similar connectivities and short metal–metal distances. However, the computations actually determine the sphalerite arrangement to be most favored.

The only remaining piece is the octahedral interstitial metal. Certainly, for transition metals, the interstitial is not an innocent spectator by simply donating electrons to the framework as observed in comparing the energy bands for Co_8S_8 and Co_9S_8 in

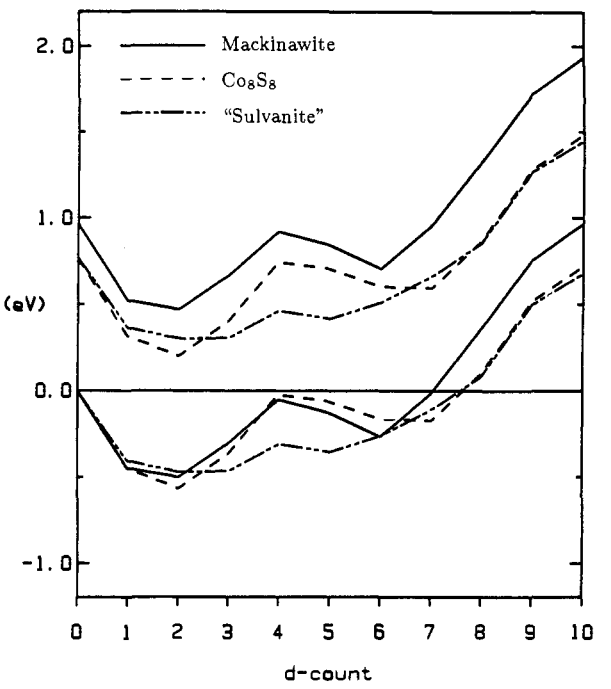

Figure 16. Energy difference curves comparing the mackinawite, Co_8S_8, and "sulvanite" structures with sphalerite. The upper three curves result directly from the calculation whereas the lower curves have their d^0 contributions removed.

Table IV. d^0 Energies for Various Structural Isomers of the Sphalerite-Type as Compounds

M_4S fragment geometry	fragment energy (eV)
tetrahedron	0.0
"inverted tetrahedron"	0.553
tetragonal pyramid	0.817
square planar	0.345

structure	frag. composition[a]	frag. energy, eV	total energy, eV
sphalerite	100% tet	0.0	0.0
pentlandite	75% tet pyr + 25% tet	0.613	0.766
mackinawite	100% tet pyr	0.817	0.970
sulvanite	100% inv tet	0.553	0.771

[a] tet = tetrahedron. tet pyr = tetragonal pyramid. inv tet = inverted tetrahedron.

Table V. Expressions for the Second and Fourth Moments for the Sphalerite Alternative Structures

structure	μ_2	μ_4
mackinawite	$8\beta_\pi^2 + 4\beta_\delta^2$	$72\beta_\pi^4 + 24\beta_\pi^2\beta_\delta^2 + 16\beta_\delta^4$
Co_8S_8	$6\beta_\pi^2 + 3\beta_\delta^2$	$30\beta_\pi^4 + 36\beta_\pi^2\beta_\delta^2 + 6\beta_\delta^4$
"sulvanite"	$6\beta_\pi^2 + 3\beta_\delta^2$	$44\beta_\pi^4 + 12\beta_\pi^2\beta_\delta^2 + 22\beta_\delta^4$

(20) Pauling, L. *The Nature of the Chemical Bond*, 3rd. ed.; Cornell University Press: Ithaca, 1960; p 445.
(21) Burdett, J. K.; Lee, S. *J. Am. Chem. Soc.* **1985**, *107*, 3050.

Figures 14 and 15. We should note that the Co_8S_8 arrangement is extremely propitious for accepting metal atoms in one-eighth of the octahedral holes in the anion packing. The sphalerite structure, on the other hand, is not conducive for introducing atoms into these voids, primarily because an unreasonably short metal–metal distance will occur between the interstitial and the host atoms. Tetrahedral holes are available and known to be occupied in the stuffed sphalerite derivatives,[22a] mooihoekite ($Cu_9Fe_9S_{16}$),[22b] haycockite ($Cu_4Fe_5S_8$),[22c] and talnakhite ($Cu_{18}Fe_{16}S_{32}$).[22d] The energy difference between Co_9S_8 in the pentlandite and mooihoekite structures constrainted to the same volume per formula unit is 1.62 eV in favor of the stuffed sphalerite. However, from Figure 16 we extract a difference of 4.74 eV between sphalerite and the defect pentlandite. The interstitial transition metal stabilizes pentlandite by 3.12 eV relative to the stuffed sphalerite. If we consider a less interacting interstitial atom, e.g., Mg, we find that the pentlandite structure becomes destabilized by an additional 0.54 eV.

Second- and Third-Row Analogues

At this point, one may wonder about the absence of these clusters for Rh or Pd, even for Ir or Pt. However, tetrahedral coordination of these heavier transition metals is extremely rare; square-planar arrangements for d^8 Rh^I, Ir^I, Pd^{II}, Pt^{II} are quite common.[23] Under careful scrutiny of the complex sulfide $Rh_{17}S_{15}$ we can discern a network of metal cubes connected via bridging sulfides.[24] In addition to one octahedrally coordinated Rh atom (d(Rh–S) = 2.336 Å, typical for Rh^{III}), the structural highlight is the trimer of square-planar Rh atoms, **15**, linked together at

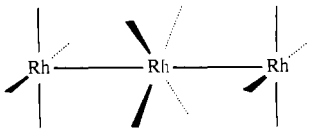

15

the terminal sulfides in a manner which maintains cubic symmetry. This Rh–Rh distance of 2.59 Å is extremely short (2.69 Å in the metal). Of the sulfides, 60% are square pyramidally coordinated while 40% feel a tetrahedral environment of metals. Of the 34 Rh atoms per unit cell, there are three trimers $[(RhS_{4/2})(RhS_{4/2})_2]$ and one octahedral Rh, $[RhS_{6/2}]$, and the remaining 24 metals constitute the network of cubes to give the structural formula $[RhS_{6/2}][(RhS_{4/2})(RhS_{4/2})_2]_3[Rh_8S_{2/2}S_{4/2}]$. Since there are no S–S contacts, we can represent the formal charges as $[(Rh_8^{x+})_3(Rh_3^{y+})_3Rh^{3+}][S^{2-}]_{30}$ and, therefore, $x + y = 19$ must be satisfied for electroneutrality. The common oxidation state for square-planar Rh is Rh^I (d^8) for which four Rh d orbitals are completely occupied. Taking into account the metal–metal interactions, the occupied d_{z^2} orbital provides the strongest overlap. From the schematic MO diagram, **16**, for this three orbital in-

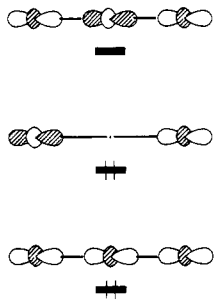

16

teraction, analogous to the allyl system, we anticipate for such short Rh–Rh distances to be observed the d_{z^2} antibonding level should be depopulated, thereby assigning $y = 5$. The resulting oxidation state for each Rh_8 cube is +14, leading to 58 d electrons, the "magic number" for transition-metal cubes. No band calculations were performed on the structure, however, due to the excessive size of the required basis set and, therefore, we are unable to corroborate these results with those for the solid.

Table VI. Parameters for Extended Hückel Calculations

	orbital	H_{ii} (eV)	$\zeta_1(c_1)^a$	$\zeta_2(c_2)^a$
V	4s	−8.81	1.30	
	4p	−5.52	1.30	
	3d	−11.00	4.75 (0.4755)	1.70 (0.7052)
Fe	4s	−9.22	1.90	
	4p	−5.37	1.90	
	3d	−12.28	5.55 (0.5366)	1.80 (0.6678)
Co	4s	−9.21	2.00	
	4p	−5.29	2.00	
	3d	−13.18	5.55 (0.5679)	2.10 (0.6059)
Ni	4s	−8.86	1.93	
	4p	−4.90	1.93	
	3d	−12.99	5.75 (0.5817)	2.20 (0.5800)
H	1s	−13.60	1.30	
C	2s	−21.40	1.63	
	2p	−11.40	1.63	
O	2s	−32.30	2.28	
	2p	−14.80	2.28	
P	3s	−18.60	1.88	
	3p	−12.50	1.63	
S	3s	−20.00	2.12	
	3p	−13.30	1.83	

[a] Exponents: double-ζ d functions are used for transition metals

Summary

The pentlandite structure involves an extremely complicated interplay of various interatomic forces. Metal–metal bonding effects confined to the cube cluster are severely affected by through-bond coupling with the face-capping sulfides. The matrix effects of the surrounding anions as well as keeping the metal–sulfur antibonding levels of the M_8S_6 rhombic dodecahedral cluster unoccupied provide rationalization for the narrow range of electron concentration. We find that the ligand environment can affect the exact number of cluster valence electrons suitable for maximum stability. With good π-donor species as capping ligands, the cluster prefers slightly fewer electrons than for π-acceptors as these ligands. Most importantly for the solid, the interstitial octahedral metals not only link the cluster units together but are crucial in stabilizing the Co_8S_8 framework. The nature of these metals best suited for the requirements of the structure include late transition metals due to their size and low chemical potentials.

Acknowledgment. This research was supported by NSF DMR 8414175 and DMR 8216892.

Appendix

All of the calculations described in this paper used the Extended Hückel method[25] both for the molecular orbital calculations on the clusters and for the tight-binding computations on the crystalline solids. The atomic parameters are listed in Table VI.

For Co_9S_8, $[Co_8S_6(SH)_8]^{4-}$, and $Ni_8(PH)_6(CO)_8$, the observed geometries were used although we performed calculations on each compound using a variety of parameter combinations and geometrical changes to ensure a consistent argument. For the energetic comparisons among the structural alternatives, we selected an idealized geometry: exact tetrahedral coordination of the transition metal, M–M distance of 2.543 Å, and M–S distances of 2.22 Å. All lattice summations were carried through second nearest-neighbor cells. For calculations of DOS and COOP curves for pentlandite, a set of 10 special points was selected for averaging over the Brillouin zone.

(22) (a) Hall, S. R. *Can. Miner.* **1975**, *13*, 168. (b) Hall, S. R.; Rowland, J. F. *Acta Crystallogr.* **1973**, *B29*, 2365. (c) Rowland, J. F.; Hall, S. R. *Acta Crystallogr.* **1975**, *B31*, 2105. (d) Hall, S. R.; Gabe, E. J. *Am. Miner.* **1972**, *57*, 368.

(23) Cotton, F. A.; Wilkinson, G. *Advanced Inorganic Chemistry*, 4th ed.; Wiley: New York, 1980.

(24) (a) Geller, S. *Acta Crystallogr.* **1962**, *15*, 1198. (b) Geller, S. *Acta Crystallogr.* **1962**, *15*, 713.

(25) (a) Hoffmann, R. *J. Chem. Phys.* **1963**, *39*, 1397. (b) Ammeter, J. H.; Bürgi, H.-B.; Thibeault, J. C.; Hoffmann, R. *J. Am. Chem. Soc.* **1978**, *100*, 3686.